Available online at www.sciencedirect.com
ScienceDirect
International Journal of Multiphase Flow 34 (2008) 690–705
International Journal of Multiphase Flow
www.elsevier.com/locate/ijmulflow

3-D numerical simulation of contact angle hysteresis for microscale two phase flow

Chen Fang *, Carlos Hidrovo, Fu-min Wang, John Eaton, Kenneth Goodson

Department of Mechanical Engineering, Stanford University, Stanford, CA 94305-3032, United States

Received 13 April 2007; received in revised form 7 August 2007

Abstract

Understanding the physics of microscale two-phase flow is important for a broad variety of engineering applications including compact PEM fuel cells and heat exchangers. The low Bond number and confined geometry make it critical to consider both the surface tension at the liquid–gas interfaces and the surface forces acting at the channel boundaries. Within the framework of a numerical volume of fluid (VOF) approach, the present work proposes a model to account for surface adhesion forces by considering the effects of contact angle hysteresis. A transient model is developed by correcting boundary force balances through specification of the local contact angle and instantaneously updating the local angle values based on the variation of the volume fraction from previous time steps. The model compares very well with new data provided here for droplets on a rotating disk and liquid slug flow in microchannel. The simulation reveals that the contact angle distribution along the slug profile in the microchannel flow can be approximated using a piecewise linear function. This study indicates that the asymmetric distribution of the contact angle might be responsible for several phenomena observed in the microchannel experiments, including slug instability.

Keywords: Contact angle hysteresis; Volume of fluid (VOF); Two-phase flow; Microscale; Droplet detachment; Liquid slug detachment

1. Introduction

Multiphase flows in microchannels have been extensively studied in the past few decades due to their wide range of applications. For instance, proton exchange membrane fuel cells (PEMFCs) operating at high current densities tend to suffer from excessive water accumulation, leading to liquid blockage of the cathode flow channel. Hence, water management that ensures the effective removal of byproduct water from the microchannel is critical (Cha et al., 2003). In addition, microscale multiphase flow also plays an important role in the microelectronics cooling technology (Peng and Wang, 1993; Zhang, 2000). MEMS technology also motivates the research on multiphase flows in microchannels. A novel gas–liquid–solid catalyzed reactor, for example, was discussed in Crynes et al. (1996).

Flow regime maps of multiphase microchannel flows reveals that in a wide range of flow conditions the bubble/slug flow is the primary flow pattern (Feng and Serizawa, 2000; Hidrovo et al., 2004). The small dimension of the microchannel leads to a small Bond Number which means that surface forces play an important role in determining the dynamics of liquid slugs and bubbles whereas body forces are generally negligible (Hidrovo et al., 2005). Furthermore, since the two-phase flow happens inside a confined space, it is critical to consider the interaction between the boundary and the fluid in-between. Specifically, the surface forces acting at the boundaries are of particular importance (Barajas and Panton, 1992).

Various numerical methods have been used in the study of multiphase flows in microchannels. A conservative method suitable for the treatment of the interface topological changes, the VOF approach is found to be among the

* Corresponding author. Tel.: +1 6502153026.
E-mail address: chenfang@stanford.edu (C. Fang).

0301-9322/$ - see front matter © 2007 Elsevier Ltd. All rights reserved.
doi:10.1016/j.ijmultiphaseflow.2007.08.008

best numerical tools when the bubble/slug dynamics and the liquid/gas interface morphology are of particular interest (Gregor et al., 2001). The velocity field and bubble profile in a vertical gas–liquid flow inside capillaries has been obtained (Taha and Cui, 2004) and it was found to be in good agreement with experimental measurements. Tseng et al. (2002) used a VOF model to analyze the filling process of liquid slugs through channel network. The simulation focused on the influence of the wall wettability and the result showed that wall surface hydrophobicity is a dominating factor in the filling processes of reservoirs.

Understanding of the surface tension acting on the contact line is of particular importance in bubble/slug flows in confined spaces. Contact angle is the critical parameter in evaluating the surface adhesive force. However, the contact angle hysteresis effect, i.e. the non-uniqueness of the static contact angle, substantially complicates the determination of angle value and is responsible for various multiphase flow phenomena at small scale. Blackmore et al. (2001), Mahe et al. (1988) and Basu et al. (1997) experimentally studied the detachment of air bubbles in a slit microchannel by a shearing flow and the balance between the liquid drag force and the surface adhesive force caused by the contact angle asymmetry was addressed. In addition to the experiment, Renardy et al. (2001) numerically simulated the moving contact line problem based on VOF model, using two methods to implement the contact angle condition. However, the contact angle needs to be either pre-determined based on Young's equation or prescribed as an input in their model, and the contact angle hysteresis effect was not addressed. To allow for the non-uniqueness of the contact angle, Theodorakakos et al. (2006) numerically studied the droplet detachment on GDL material by correlating the real contact angle value with the contact line velocity. Similarly, Chen et al. (2008) and Francois and Shyy (2003) assumed that the real contact angle is a linear function of contact line velocity. However, such model may cause unphysical behavior, e.g. the contact point can move backward even when the contact line velocity is positive, due to the fact that the real contact angle depends on not only the current flow state, but also the history of the contact line motion. Unfortunately, there is a lack of numerical tools to analyze the influence of the contact angle hysteresis effects on microchannel flows by accounting for the contact line motion history.

The present study proposes a 3-D contact angle hysteresis model within the framework of the VOF approach. Upon solving the non-linear equations relating the volume fraction, interface position, and contact angle, a special algorithm is developed to replicate the hysteresis effect based on considering the contact line movement history. The model is validated against data from two experiments on droplet/slug dynamics, and quantitative matching is achieved for a wide range of flow conditions. The simulation indicates the importance of considering the surface adhesive force and the contact angle hysteresis effect for microscale multiphase flow. The results also reveal that the contact angle distribution along the liquid slug profile could be approximated using a piecewise linear function. Moreover, the contact angle asymmetry is found responsible for the slug elongation and the post-detachment slug instability.

2. Contact angle hysteresis effect

By assuming constant surface tensions between each pair of the three phases, the well-known Young's equation is expressed as

$$\sigma_{LG}\cos\theta_s = \sigma_{GS} - \sigma_{LS} \tag{1}$$

Young's equation relates the experimentally measurable parameters θ_s and σ_{LG} to σ_{GS} and σ_{LS}, which are generally not available experimentally. For constant surface tensions of the three phases, Eq. (1) implies that the static contact angle θ_s is unique. However, this implication contradicts the experimental observations that for most material systems, the real contact angle θ can take on any value within the interval $\theta_R \leqslant \theta \leqslant \theta_A$ and that the contact line remains fixed for angle variations within this range, a phenomenon typically referred to as the contact angle hysteresis. Various modifications to Young's equation have been proposed to account for the contact angle hysteresis effect, and a comprehensive review on this topic was given by Dussan (1979). Although the mechanism governing contact angle hysteresis remains an open topic, we can circumvent this difficulty in the numerical simulation by considering three length scales, as shown in Fig. 1. The largest length scale illustrated in the figure is the mesh scale, based on which the numerical discretization is performed. Here, σ_{NET} represents the net force exerted by the solid wall on the interface. Generally, σ_{LG} is measurable experimentally whereas σ_{NET} must be determined by indirect methods. The surface tensions of the three phases are all constants over the mesh scale. By zooming in the area near the contact line on the mesh scale, we move onto the experimental observation scale (Fig. 1b), which is much larger than the molecular mean free path, so the surface tension remains constant over this scale. Meanwhile, the observation scale is much smaller than the droplet/bubble surface curvature, hence the interface can be simply treated as a flat plane, as indicated in Fig. 1b. Such scale corresponds to the smallest scale available in the experimental observation, and the effective contact angle θ_s measured by drawing the tangential line at the contact point should be defined at this scale. Applying the x-component force balance to the interface at the observation scale yields:

$$\sigma_{LG}\cos\theta_s = \sigma_{NET} \tag{2}$$

which means that we can use the experimentally measured effective contact angle θ_s to correlate the known surface tension σ_{LG} with the unknown σ_{NET}. Moreover, since the surface tension remains constant when we zoom out from the observation scale back to the computational mesh scale, Eq. (2) still holds on at the mesh scale, and we can

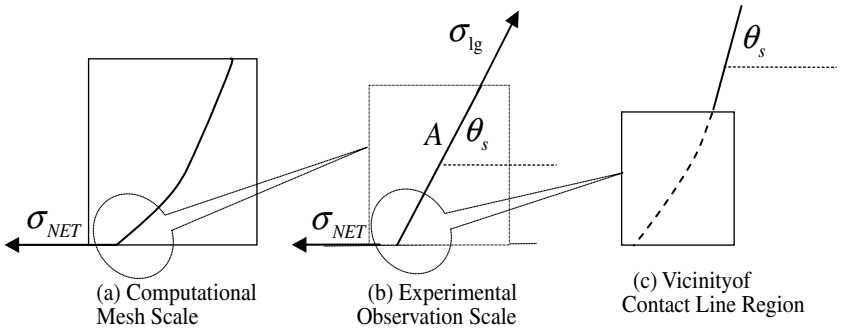

Fig. 1. Comparison of three length scales. The simulation is performed at the computational mesh scale, the effective contact angle θ_s is defined at the observation scale, while in the vicinity of the contact line region, the three phases overlap and the definitions of the contact line and contact angle become ambiguous.

directly use the experimentally measured effective contact angle θ_s in the mesh cell located at the contact line to evaluate σ_{NET}. When we zoom in from the observation scale to the vicinity of the contact line region (Fig. 1c), which extends a few molecular diameters from the solid surface, the continuity assumption breaks down, and the definition of liquid gas interface and the contact angle becomes ambiguous. However, θ_s is defined outside of this scale. Recognizing that the physics within the contact line region results in the complexity of the contact angle hysteresis, we have circumvented the difficulty by experimentally measuring the effective contact angle θ_s, based on which σ_{NET} is determined.

A basic hysteresis process can be described as that the contact line remain fixed at a given position, provide the value of the contact angle θ lies within the interval $\theta_R \leqslant \theta \leqslant \theta_A$, where θ_R and θ_A are defined as the advancing and receding angles, respectively. Here, the advancing/receding contact angle only refers to the equilibrium values. In actuality, it is found experimentally that once the contact line starts to move, the contact angle will deviates from the equilibrium value. As shown in Fig. 2, a wetting process with a positive contact line velocity causes the contact angle to positively deviate from the equilibrium advancing angle, while a dewetting process results in a negative deviation. Many empirical correlations relating contact angle

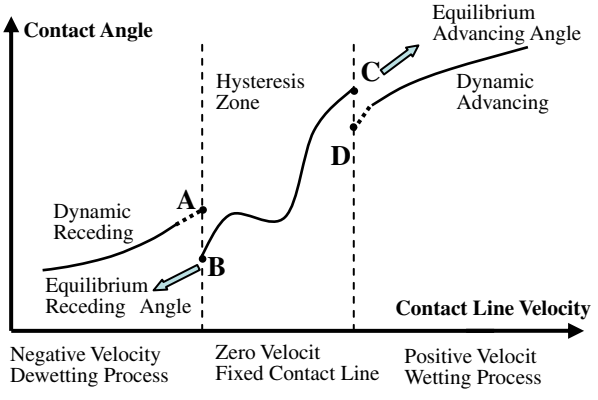

Fig. 2. Map of contact angle versus contact line velocity.

with capillary number have been proposed, among which are the Hoffman–Jiang correlation for advancing contact angle (Jiang et al., 1979):

$$\frac{\cos\theta_{adv}-\cos\theta_d}{\cos\theta_{adv}+1}=\tanh(4.96Ca^{0.702}),\quad \text{when } 10^{-3}<Ca<1,\quad We<10^{-3},\quad Bo<10^{-1} \tag{3}$$

and the Hoffman–Tan law for the receding contact angle (Tanner, 1979):

$$\theta_{rec}^3-\theta_d^3=C_T Ca \tag{4}$$

where C_T is a constant. θ_{rec}, θ_{adv} are the equilibrium advancing and receding contact angles, respectively. Considering their simple form, Eqs. (3) and (4) are used in the present study. A numerical evaluation of Eqs. (3) and (4) shows that at moderately low contact line velocities the dynamic contact angle is very close to its equilibrium counterpart and the deviation is negligible. In fact, measurements on slowly moving drops have been used for the purpose of determining equilibrium contact angles (Rotenberg et al., 1984).

3. Numerical model

3.1. VOF model

The VOF method is employed here for the numerical investigation of the microscale two-phase flow because it allows tracking of immiscible interfaces and calculation of the surface tension. The two-fluid flow is modeled with the Navier–Stokes equation:

$$\rho\left(\frac{\partial u}{\partial t}+(u\cdot\nabla)u\right)=-\nabla p+\nabla\cdot(\mu S)+f \tag{5}$$

where ρ, μ and f are the density, viscosity, and body force term of the momentum equation, respectively. The quantity S is the rate of strain tensor

$$S_{ij}=\frac{1}{2}\left(\frac{\partial u_j}{\partial x_i}+\frac{\partial u_i}{\partial x_j}\right) \tag{6}$$

In our calculations, the body force f includes the gravity and interfacial tension. The velocity field u is subject to the incompressibility constraint

$$\nabla \cdot u = 0 \tag{7}$$

In the VOF method, the motion of the interface between immiscible liquids of different density and viscosity is defined by a phase indicator – the volume fraction function α. To allow for mass conservation of each phase, an additional equation is introduced:

$$\frac{\partial \alpha}{\partial t} + u \cdot \nabla \alpha = 0 \tag{8}$$

We use (8) to represent and track the interface which is transported by the velocity field u. Moreover, the averaged values of the density and the viscosity are calculated with the volume fraction:

$$\begin{aligned} \rho &= \alpha \rho_1 + (1-\alpha)\rho_2 \\ \mu &= \alpha \mu_1 + (1-\alpha)\mu_2 \end{aligned} \tag{9}$$

The current VOF model employs the Marker and Cell (MAC) finite difference method, which is based on the use of rectangular grids. Nodal values of the volume fraction C and the pressure p are defined at the center of each cell, while the nodal values of the horizontal and vertical velocity components are defined at the midpoints of the vertical and horizontal sides, respectively. In each time step the volume fraction α, which indicates the two-phase interface position, is first updated and then followed by the calculation of the surface tension. Finally, the velocity and pressure fields are solved based on the Navier–Stokes equation.

Updating of the interface location is based on Young's piecewise linear interface construction (PLIC) scheme (Youngs, 1982), in which the normal vector n of the interface is first related to the gradient of volume fraction by $n = \nabla C/|\nabla C|$. Then, a flat plane having a normal vector n is used to approximate the real liquid–gas interface within each cell. With the knowledge of the interface position change, the volume of fluid transferring into the neighboring cells is evaluated and the volume fraction α updated.

Due to the small Reynolds number which is typical of microscale flows, a laminar flow model is used. The equations are solved by an algebraic multigrid (AMG) solver (Issa et al., 1991), and the pressure-implicit with splitting of operators (PISO) scheme for pressure–velocity coupling.

3.2. Surface tension calculation and contact angle determination

The Young–Laplace equation expresses the surface tension in terms of the surface curvature k, surface tension coefficient σ, as well as the surface normal $\hat{n}$:

$$f = \sigma k \hat{n} \tag{10}$$

In our simulation, surface tension is applied using the continuous surface force (CSF) scheme (Brackbill et al., 1992).

The addition of surface tension to the VOF method is modeled by a source term f in the momentum equation:

$$f = \sigma k \frac{2\rho}{\rho_1 + \rho_2} \nabla \alpha \tag{11}$$

where ρ is given by Eq. (9). In our present treatment, σ is simply a constant and Maragoni effects are not considered. The curvature k is defined in terms of the divergence of the unit normal n:

$$k = -(\nabla \cdot \hat{n}) = -\left[\nabla \cdot \left(\frac{1}{|\nabla \alpha|} \nabla \alpha\right)\right] \tag{12}$$

$$\text{where } \hat{n} = \frac{n}{|n|} \tag{13}$$

Substituting (12) into (11), yields:

$$f = 2\sigma\rho \frac{\nabla \alpha}{\rho_l + \rho_g} \frac{1}{|\nabla \alpha|} \left[\left(\frac{\nabla \alpha}{|\nabla \alpha|} \cdot \nabla\right)|\nabla \alpha| - (\nabla^2 \alpha)\right] \tag{14}$$

In applying formulation (14), a Marker and Cell (MAC) like discretization scheme is used. A unit vector n is calculated from discretizing the volume fraction α of the immediate 26 neighboring cells, based on the relation $n = \nabla \alpha$. Initially, a cell corner value of the normal vector is computed. Then required cell-centered values are given by averaging the corner values. Also, $\nabla^2 \alpha$ is calculated by discretizing the normal vector values obtained at the eight cell corners.

The corner normal vector of the cell located at the boundary is determined by directly applying the contact angle boundary condition instead of by discretizing the α values of neighboring cells. Here, the surface normal $\vec{n} = [n_x, n_y, n_z]$ at the contact line is first determined by recognizing that $n_y/\sqrt{n_x^2 + n_z^2} = \cot\theta$, where θ is the contact angle. Then the obtained contact line normal is assigned to the four cell corners lying on the boundary as shown in Fig. 3.

Some modification is needed if we apply the above-mentioned methodology to the interface at the corner. Assume the interface is at angles α and β with respect to the bottom and side wall boundaries, respectively (Fig. 4). Upon applying the geometric relationship it is found that the normal of the interface (shaded plane in Fig. 4) $\vec{n} = [1, A, B]$ is given by:

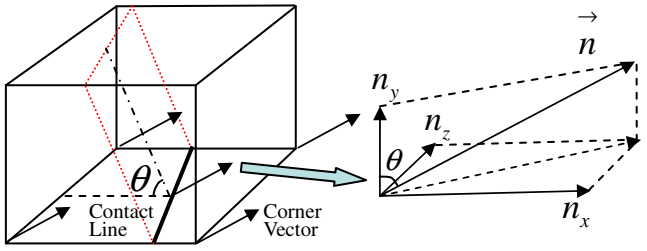

Fig. 3. Corner vector evaluation for boundary cell by contact angle specification.

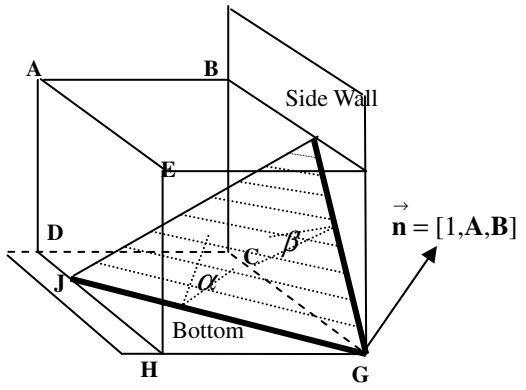

Fig. 4. Contact angle specification at corner cell.

$$A^2 = \frac{\cos^2\alpha}{1-\cos^2\alpha-\cos^2\beta} \tag{15}$$

$$B^2 = \frac{\cos^2\beta}{1-\cos^2\alpha-\cos^2\beta} \tag{16}$$

The presence of the square numbers A^2, B^2 in Eqs. (15) and (16) requires that the right-hand terms be positive. Considering a special case in which both the side wall and bottom have the same contact angle, the aforementioned constraint implies that both angles must be higher than 45°, i.e. $\alpha = \beta \geqslant 45°$, to allow the stable existence of the interface at the corner. This implication is consistent with the experimental observations shown in Concus and Finn (1974) which states that a spontaneous rising up to the top of the container occurs for the liquid in the corners provided the contact angle is small.

3.3. Numerical evaluation of local contact angle

Subsequent to knowledge of the contact angle hysteresis effect, the objective is the replication of the hysteresis process in the 3-D numerical simulation. It should be realized that a typical hysteresis process always has a memory effect in the sense that the value at the current time step depends on the parameters not only in the current time step but also in the previous time steps, i.e. its history. Here, we update the local contact angle in the current time step by considering its counterpart in the previous time step as well as the angle increment between the consecutive time steps. Specifically, the angle value θ^{i+1} at time step $i+1$ could be expressed as

$$\theta_j^{i+1} = \theta_j^i + H(\theta_j^i - \theta_{\text{rec}})H\left(\theta_{\text{adv}} - \theta_j^i\right)\frac{\partial\theta_j}{\partial\alpha_j}\triangle\alpha_j \tag{17}$$

where the Heaviside function H is defined as:

$$H(k) = \begin{cases} 1, & @\ k > 0 \\ 0, & @\ k \leqslant 0 \end{cases} \tag{18}$$

The subscript j denotes the cell j with the local contact angle θ_j. The second right-hand term of Eq. (17) represents the angle increment between time step $i+1$ and i. The volume fraction α_j, a measure of the liquid/gas volume ratio in cell j, is introduced into the increment term to account for the fact that the contact angle variations are essentially caused by the change of liquid/gas volume in each cell. In deriving Eq. (17) it is realized that the advancing and receding contact angles can be viewed as the upper and lower limits of the real contact angle value, respectively. Within the range of receding and advancing contact angle, the local contact angle can vary freely whereas the contact line is pinned, while outside this range the local contact angle will be fixed at either the advancing or receding angle with a moving contact line and the increment term in Eq. (17) simply drops out.

Eq. (17) still requires the evaluation of $\partial\theta_j/\partial\alpha_j$. Here, a rectangular cell lying on the boundary is considered (Fig. 5). In the VOF model, the liquid–gas interface is approximated as a plane within each cell, as indicated by plane A–B–C–D–E–F in the graph. Also, the triple contact line where three phases make contact is represented by the intersecting line of the interface plane and the bottom plane, as highlighted by the red[1] dashed line in Fig. 5, where the contact angle θ is also shown. In accordance to the definition of contact angle, the volume fraction α corresponds to the volume of the portion of the cell below the interfacial plane. As discussed previously, the contact line should be fixed during the variation of α, provided θ lies between the advancing and receding angle values. Therefore, a change of α simply results in the rotation of the interfacial plane A–B–C–D–E–F about the axis BH to, say, either A′–B′–C′–D′–E′–F′ (α increases) or A″–B″–C″–D″–E″–F″ (α decreases). In practice, the contact line could be located at any position, making it necessary to derive a universal expression of $\partial\theta_j/\partial\alpha_j$ applicable to any possible geometric configuration. Assuming the surface normal of the interfacial plane A–B–C–D–E–F is $\vec{n} = [m_1, m_2, m_3]$, then the equation of the plane is;

$$m_1x + m_2y + m_3z = \beta \tag{19}$$

It is further assumed that $0 < \theta < 90°$, m_1, m_2, $m_3 \geqslant 0$ (this condition can always be satisfied by appropriate coordinate transformation). Let $g = m_2/m_1$, $h = \beta/m_1$, $f = m_3/m_1$, substituting into Eq. (19) yields:

$$x + gy + fz = h \tag{20}$$

The volume fraction α can be expressed as

$$\begin{aligned}\alpha = \frac{1}{6gh}\Bigg[&h^3 - \sum_{j=1}^{3} H\left(h - \frac{m_jC_j}{m_1}\right)\left(h - \frac{m_j}{m_1}\right)^3 \\ &+ \sum_{j=1}^{3} H\left(h - C_1 - gC_2 - fC_3 + \frac{m_jC_j}{m_1}\right) \\ &\times\left(h - C_1 - gC_2 - fC_3 + \frac{m_jC_j}{m_1}\right)^3\Bigg]\end{aligned} \tag{21}$$

[1] For interpretation of color in Fig. 6, the reader is referred to the web version of this article.

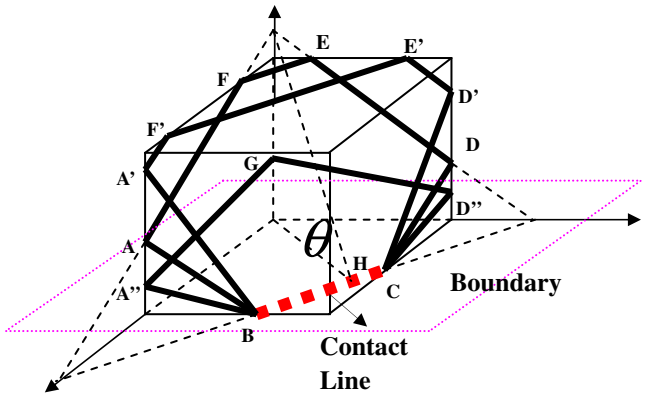

Fig. 5. Calculation of $\partial\theta_j/\partial\alpha_j$ when contact line is fixed.

where the Heaviside function H is defined in Eq. (18). C_j refers to the length of the rectangular cell edge. Observing that $m_3 = \sqrt{m_1^2 + m_2^2}/\tan(\theta)$, α can be expressed in terms of the contact angle θ as

$$\begin{aligned}\alpha &= \alpha(g,h,\theta)\\ &= \frac{1}{6gh}\left[h^3 - \sum_{j=1}^{3} H\left(h - \frac{m_j C_j}{m_1}\right)\left(h - \frac{m_j}{m_1}\right)^3 \right.\\ &\quad + \sum_{j=1}^{3} H\left(h - C_1 - gC_2 - \frac{\sqrt{1+g^2}}{\tan\theta}C_3 + \frac{m_j C_j}{m_1}\right)\\ &\quad \left.\times\left(h - C_1 - gC_2 - \frac{\sqrt{1+g^2}}{\tan\theta}C_3 + \frac{m_j C_j}{m_1}\right)^3\right]\end{aligned} \tag{22}$$

Finally, we have

$$\left.\frac{\partial\alpha}{\partial\theta}\right|_{\text{fixed contact line}} = \left.\frac{\partial\alpha}{\partial\theta}\right|_{g,h} = A + B + C \tag{23}$$

where

$$\begin{aligned}A &= \frac{\sec^2\theta}{6g\sqrt{1+g^2}}\left[h^3 - \sum_{j=1}^{3} H\left(h - \frac{m_j C_j}{m_1}\right)\left(h - \frac{m_j}{m_1}\right)^3 \right.\\ &\quad + \sum_{j=1}^{3} H\left(h - C_1 - gC_2 - \frac{\sqrt{1+g^2}}{\tan\theta}C_3 + \frac{m_j C_j}{m_1}\right)\\ &\quad \left.\times\left(h - C_1 - gC_2 - \frac{\sqrt{1+g^2}}{\tan\theta}C_3 + \frac{m_j C_j}{m_1}\right)^3\right]\end{aligned}$$

$$B = \frac{-\csc^2\theta\tan\theta C_3\sqrt{1+g^2}}{6g\sqrt{1+g^2}}\left[3(h - fC_3)^2 H(h - fC_3)\right]$$

$$\begin{aligned}C &= \frac{\tan\theta}{6g\sqrt{1+g^2}}\left[3H(h - gC_2 - fC_3)\right.\\ &\quad \times\left(h - gC_2 - C_3\sqrt{1+g^2}/\tan\theta\right)^2\left(\csc^2\theta\sqrt{1+g^2}C_3\right)\\ &\quad + 3H(h - C_1 - fC_3)\left(h - C_1 - C_3\sqrt{1+g^2}/\tan\theta\right)^2\\ &\quad \left.\times\left(C_3\csc^2\theta\sqrt{1+g^2}\right)\right]\end{aligned}$$

Based on Eq. (23), $\partial\theta_j/\partial\alpha_j$ and the angle increment can be calculated for each cell containing the contact line in each time step. Finally, the contact angle in time step $i+1$ can be readily updated based on the information in time step i, using Eq. (17).

The contact angle update approach discussed above is virtually a forward Euler method. If the location of the contact line is very close to the cell corner, the derivative $\partial\theta_j/\partial\alpha_j$ can attain extremely high values resulting in a significant error when using Euler method. An alternative approach is to directly solve the non-linear equation (22), which relates the contact angle θ_j^{i+1} in the next time step with α_j^i as well as g,h indicating the contact line position in the current time step. The position of the contact line can be determined in the manner given by Scardovelli and Zaleskiy (2000). Here, assuming the equation for the interfacial plane takes the form of Eq. (19) and the primary phase volume is given by α and that $\alpha \leqslant 0.5$ (otherwise, a coordinate transformation is needed), and that $\beta^* = \beta/m_1C_1 + m_2C_2 + m_3C_3$, $m_{12} = m_1 + m_2$, and $m = \min(m_{12}, m_3)$, then β^* can be calculated as follows:

$$\begin{aligned}&\beta^* = \sqrt[3]{6m_1m_2m_3\alpha} \quad \text{for } 0 \leqslant \alpha \leqslant \alpha_1\\ &\beta^* = 0.5(m_1 + \sqrt{m_1^2 + 8m_2m_3(\alpha - \alpha_1)}) \quad \text{for } \alpha_1 \leqslant \alpha \leqslant \alpha_2\\ &\qquad -\beta^{*3} + 3m_{12}\beta^{*2} - 3(m_1^2 + m_2^2)\beta^* + m_1^3 + m_2^3\\ &\qquad -6m_1m_2m_3\alpha = 0 \quad \text{for } \alpha_2 \leqslant \alpha \leqslant \alpha_3\\ &\qquad -2\beta^{*3} + 3\beta^{*2} - 3(m_1^2 + m_2^2 + m_3^2)\beta^*\\ &\qquad +m_1^3 + m_2^3 + m_3^3 - 6m_1m_2m_3\alpha = 0 \quad \text{for } \alpha_{31} \leqslant \alpha \leqslant 0.5\\ &\beta^* = m_3\alpha + m_{12}/2 \quad \text{for } \alpha_{32} \leqslant \alpha \leqslant 0.5\end{aligned} \tag{24}$$

Since the contact line is fixed when α changes, β^* and hence g,h for time step i are substituted into Eq. (22) to obtain the updated contact angle in time step $i+1$. The derivative $\partial\alpha/\partial\theta$ has been given by Eq. (23), so the non-linear equation (22) can be readily solved using the Newton–Rhapson iteration method. However, the right-hand term of Eq. (22) is periodic in terms of θ due to the presence of the trigonometric functions, resulting in the non-unique solutions. To ensure the convergence to the interval $[0,\pi]$ which is of interest here, Eq. (22) is modified to be a piecewise function when applying the Newton method:

$$\begin{aligned}&\alpha = \alpha(g,h,\pi) + \theta - \pi \quad \text{if } \theta > \pi\\ &\alpha = \alpha(g,h,\theta) \quad \text{if } \theta \in [0,\pi]\\ &\alpha = \alpha(g,h,0) + \theta \quad \text{if } \theta < 0\end{aligned} \tag{25}$$

Then the solution to the modified Eq. (25) becomes unique and the convergence to $[0,\pi]$ is guaranteed.

In practice, the contact angle value is stored and updated for each cell on the contact line. Since the mesh is fixed in VOF model, the contact angle value in the previous time step may become unavailable if the contact line is shifting from one cell to another. To solve this problem, the local contact angle values of the cells lying on the contact line (cell B in Fig. 6) are dynamically passed to their

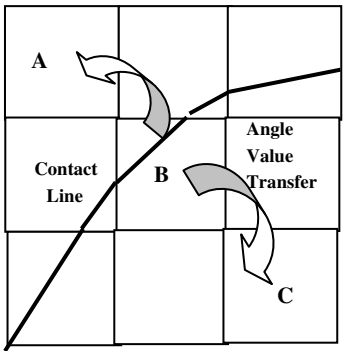

Fig. 6. Schematic of contact angle value transfer to neighboring cells.

neighboring cells located in the normal direction of the contact line (cells A and C).

As illustrated in Fig. 2, the hysteresis effect no longer influences the contact angle value provided the contact line is in motion. Instead, the contact angle becomes a function of the contact line velocity. Therefore, the use of Eqs. (3) and (4) to solve for the contact angle value requires knowledge of the contact line velocity. Since the contact line location is given by Eq. (24), the displacement of the contact line between two consecutive time steps can be deduced and the contact line velocity can be readily calculated as well.

3.4. Computational domain and boundary conditions

In the present study, two categories of water–air multiphase problems are simulated using the hysteresis model: (1) small droplet detachment on a rotating disk, and (2) slug flow in a square microchannel. Both of them are specially selected to highlight the influence of the surface tension and contact angle hysteresis effects and their details are given in Section 4.

For the case of a droplet on a rotating disk, a rectangular parallelepiped cavity of 10 mm × 10 mm × 10 mm is employed in which the air–water transport process is modeled as a transient two-phase problem (Fig. 7a). No-slip boundary condition is applied to the cavity bottom on which the droplet is placed. A velocity inlet boundary condition (uniform velocity normal to the inlet) was applied to a 0.2 mm × 0.2 mm water inlet at the center of the cavity bottom to generate droplet growth. The rest of the five interior walls of the cavity are assigned as outlet flow condition (the gradients of all flow parameters are zero).

For the microchannel slug flow problem, a straight channel 5 mm in length with rectangular cross-section of 500 μm × 45 μm is used as the computation domain (Fig. 7b). The no-slip boundary condition is applied to all the microchannel walls. A velocity inlet boundary condition was specified at both the air inlet located at the one end of the microchannel and the water inlet located at the bottom of the microchannel two-thirds of the way downstream from the air inlet. Similarly to the previous problem, the boundary condition was assigned as outlet flow (zero gradients) at the channel outlet.

3.5. Numerical accuracy

In the present study, a 3-D structured orthogonal grid with about 240,000 computation nodes was employed. The node numbers in X, Y, and Z directions are 400, 30, and 20, respectively. The grid independency was validated by performing different numerical simulations for one slug flow case with varying number of nodes. This grid has been refined triple by increasing the number of cells by 20%, 40%, and 100% in every direction, respectively. Simulation results showed that the difference between 320,000 and 78,000 is minor. Considering that the computational cost increases fastly with the node number, the computational grid with 120,000 nodes was adopted for all simulation cases presented in this study. Fig. 8 shows the liquid slug profile calculated on the three grids at the detachment point for a typical flow condition.

4. Experimental setup for model validation

4.1. Measurements of droplets on a rotating disk

To establish confidence in the numerical model, the deformation and detachment process of water droplets

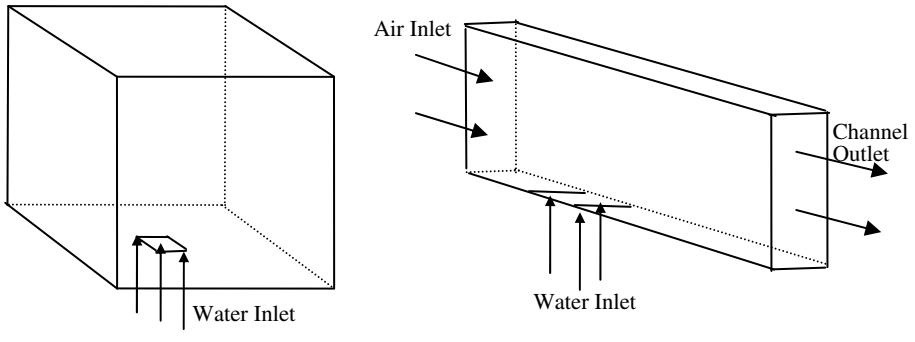

a) Droplet on plate b) Water slug in micro channel

Fig. 7. Sketch of calculation domain and boundaries (not drawn to scale).

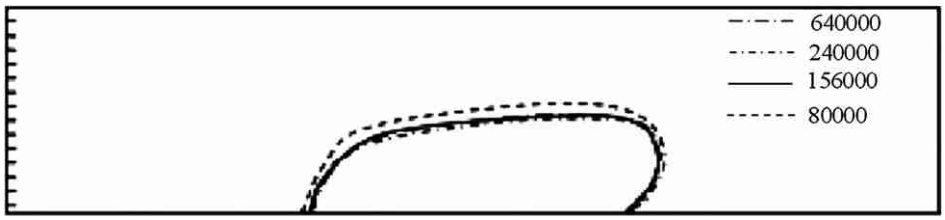

Fig. 8. Slug profile at detachment point for three different grid resolutions, flow condition: air: 15.56 m/s, water: 0.09 m/s, side wall 135°/70°, bottom: 105°/70°.

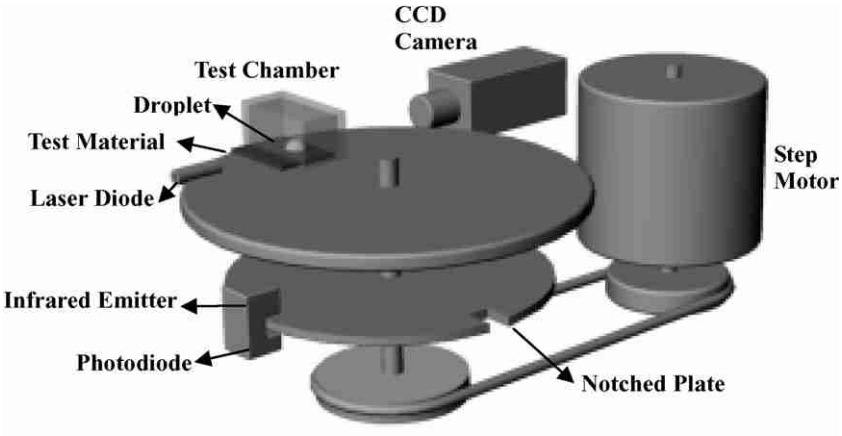

Fig. 9. Schematic of spinning plate setup. This experiment uses acceleration force to induce contact angle asymmetry.

on a spinning plate is experimentally studied and compared with the numerical prediction. In this case, a small water droplet is placed on the circular plate rotating at a designated velocity. The surface force caused by the asymmetric distribution of contact angle along the contact line balances the centrifugal force prior to detachment, until the velocity is increased to a level at which the droplet deformation reaches its limit, i.e. the contact angles at the fore and aft triple points of the liquid slug take on the advancing and receding contact angles, respectively.

Fig. 9 illustrates the basic architecture of the experimental setup. Test materials differing in surface properties are attached to a circular plate driven by a two-phase stepper motor, which precisely control the speed of the plate. The droplet is placed in an enclosed test chamber, which not only maintains the humidity of the surrounding air and suppresses the evaporation, but also isolates the droplet from the spinning-induced airflow. A Roper Scientific 12-bit CoolSNAP ES CCD camera is employed for image acquisition. A trigger system composed of an infrared emitter, a photodiode, and a notched plate is used to synchronize the camera and plate, allowing for capturing of the droplet side view at a consistent and identical imaging angle for all plate revolutions. The illumination is provided by a laser diode located behind the droplet. Before each testing, given volume of water is deposited on the test material using a thin needle connected to a syringe pump. Then the velocity of the plate is increased in a stepwise manner from zero to the detachment velocity, at which point the droplet starts to move. For each velocity step, the triggering circuit is enabled once and the corresponding droplet side view image is captured by the CCD camera. To facilitate the identification of the liquid slug detachment point, as well as to minimize the tangential acceleration which tends to deform the droplet in an unfavorable circumferential direction, the plate velocity is increased at a rate as small as 0.2 rad/s. The effective centrifugal acceleration acting on the droplet is evaluated based on the angular velocity of the plate and the distance between the droplet and rotation axis.

4.2. Measurement of slug flow in a microchannel

In addition to the spinning plate experiments, the present hysteresis model was further validated against liquid slug flow in microchannels with sidewall water injection. Here, a silicon based test structure was fabricated consisting of a U-shaped microchannel and a water reservoir connected by side slots, allowing for sidewall water injection (as shown in Fig. 10a). The channel is etched to 45 μm depth and 500 μm in width. Air flows through the microchannel while the water is injected into the microchannel through a 20 μm wide side slot located two-thirds of the way downstream from the microchannel air inlet. In order to render the microchannels hydrophobic, Molecular Vapor Deposition (MVD) of Self-Assembled Monolayers (SAMs), such as FTDS, is performed. The samples processing was carried out by Applied Micro Structures Inc.

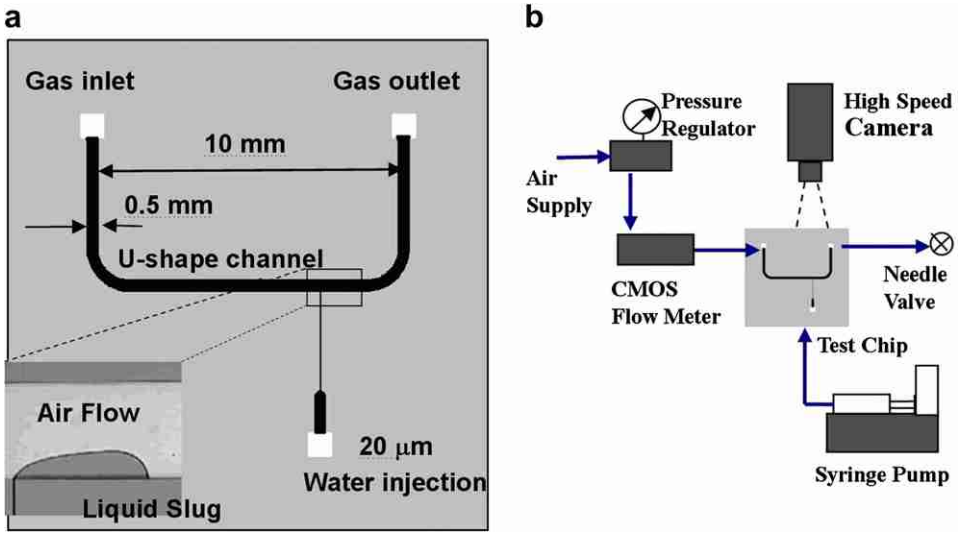

Fig. 10. (a) Image of microfabricated silicon channel. (b) Schematic of experimental setup.

(AMST) and the measured advancing contact angle was 135°. Compressed air is supplied to the microchannel and the flow rate is precisely controlled by a current operated pressure regulator (ControlAir Type-500X). A Harvard syringe pump is employed to inject the water into the microchannel at designated flow rates in the direction normal to the airflow. Depending on syringe size, water rates ranging from 1 nL/h to 0.5 mL/s can be achieved with reasonable accuracy. Also, the setup utilizes a Sensirion flow meter based on CMOS technology to monitor the air flow rate. The visualization system includes a Nikon TE2000U inverted epifluorescence microscope with 4X objectives, and a Phantom v6.1 high speed CCD camera. A frame rate of 5000 frames/s was employed to capture the dynamic slug behavior in the microchannel.

5. Results and discussion

5.1. Droplet deformation and detachment on a spinning plate

In the present study, droplet detachment on four materials, including coated silicon wafer, GDL with 0%, 5%, and 10% Teflon, are tested. The silicon wafer is rendered hydrophobic by the MVD described before. The hydrophobicity of the GDL, a porous material widely used in PEM fuel cells, increases with the concentration of the added Teflon. Before each round of test, all materials are cleaned with alcohol and dehydrated in the oven for 30 min to remove contaminants. A thin needle is used to deposit droplets of different sizes on the test material. Due to the outward motion of the contact line in the drop-forming process, the contact angle is uniformly equal to the advancing contact angle. On each material, the detachment processes is recorded for droplets of various volumes, ranging from 1.8 μL to 8 μL, and the corresponding detachment plate velocities are recorded from which the centrifugal forces acting on the droplets can be evaluated. The contact angles on both sides of the static droplet are approximately equal to the advancing contact angle (image 1 in Fig. 11 row 1). With the increase of velocity, the angle on the side closer to the rotation axis decreases until it reaches the receding angle value at the detachment point (image 5 in Fig. 11 row 1), whereas the angle on the other side remains at the advancing contact angle. Therefore, the equilibrium advancing and receding angles can be determined from the side view images captured at the detachment point by drawing a line passing through the contact point and tangent to the droplet profile.

It was found that for all the droplets, the variation of the measured contact angles for a given material was within ±1°. Table 1 shows the measured advancing and receding angles for the four materials tested. For each case the measurement is repeated six times and the mean value and its uncertainty is shown in the table. It is found that the GDL with 0% Teflon has the highest hysteresis, i.e. the difference between the advancing and receding contact angles, among the four materials, whereas higher Teflon content gives rise to a larger advancing contact angle value.

In the simulation, the same initial droplet sizes are used and the measured advancing and receding contact angles are used as input to the model. In accordance with the experiment, the centrifugal acceleration in the simulation increases in a sufficiently slow manner (0.2 rad/s^2) such that the droplet deformation can be viewed as a quasi-static process, and therefore at each point in time the droplet is in mechanical equilibrium. In practice, oscillation of the droplet may occur when the centrifugal acceleration changes. However, these oscillations are quickly damped by the liquid water viscous forces, eventually leading to a stable droplet shape for each given acceleration value, provided the process is slow enough.

Fig. 11 shows the comparison between experiments and simulations for 1.2 mm in diameter droplet on a GDL with 5% Teflon. Rows 1 through 4 illustrate the experimental

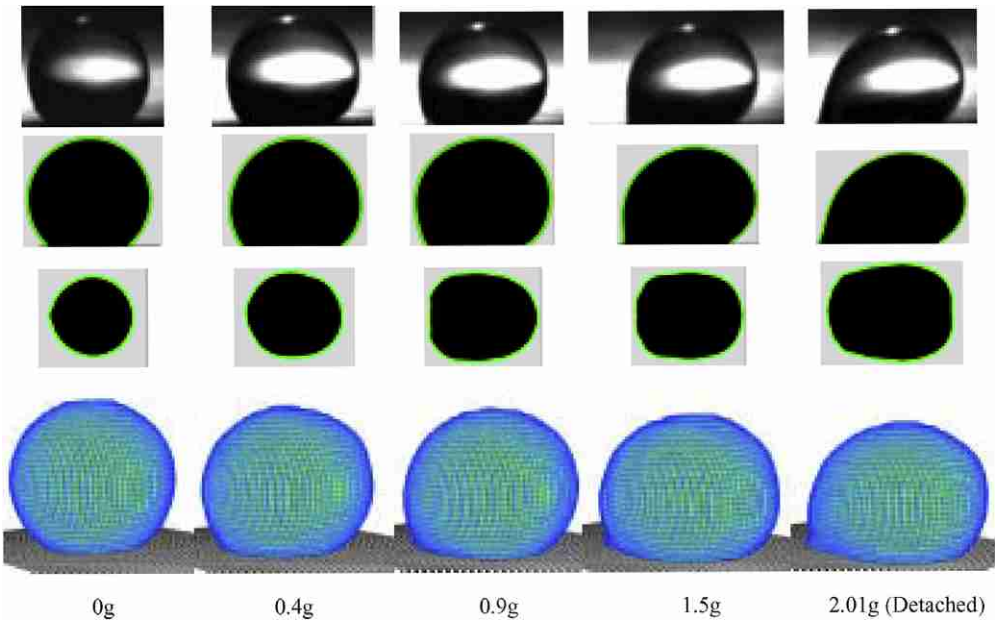

Fig. 11. Detachment process for 1.2 mm droplet on GDL with 5% Teflon, corresponding to various centrifugal accelerations (row 1: experiment, row 2: side view of simulation, row 3: contact line of simulation, row 4: perspective view of simulation).

Table 1
Measured contact angle of test materials

	Coated silicon	GDL (0% Teflon)	GDL (5% Teflon)	GDL (10% Teflon)
Adv angle	105.0° ± 1.1°	124.6° ± 0.9°	144.0° ± 1.1°	149.6° ± 0.8°
Rec angle	65.0° ± 1.2°	36.8° ± 0.9°	91.0° ± 1.3°	116.2° ± 1.5°

results in terms of the side view, contact line and perspective view of the numerically computed droplet, respectively. The sequences of images in each row correspond to increases in centrifugal acceleration from 0 to 2.01 g, at which point the droplet detaches. The numerically predicted droplet deformations for the different centrifugal acceleration values are in excellent agreement with the experiments. In response to the centrifugal force, the droplet tends to spread on the surface with its length increasing and its height decreasing.

Due to the opacity of the test material, optical observations of the contact line shape are currently not available. However, the numerical simulation shows that the contact line evolves in an interesting manner, as indicated in row 3, Fig. 11. Initially, the contact line is circular (image 1). With the increase in the centrifugal acceleration, the fore portion of the droplet advances, giving rise to a shape tapered in the direction of the motion (images 2–3). However, a further increase in acceleration causes the front part of the contact line to widen in addition to its forward movement. As a result, the contact line shifts to a shape consisting of two semi circular arcs joined by parallel sides (image 4). The width of the front part keeps increasing with the acceleration until the onset of detachment, eventually resulting in a contact line which is reversely tapered and wide at the front (image 5). In the entire process, the contact line elongates and widens significantly, and the original fore-aft symmetry is lost. Bikerman (1965) experimentally studied the evolving shape of the contact line for initially axisymmetric drops place on an inclined surface. Rotenberg et al. (1984) numerically predicted the droplet deformation on an inclined plate based on minimizing the free potential energy of the drop. Both studies showed that an elongated contact line appears in response to the gravitational force field, which is verified by the present simulation.

Fig. 12 shows the plot of critical centrifugal acceleration (the smallest acceleration inducing detachment) versus the droplet volume for the four materials tested. Both experimental results (dots) and numerical results (lines) show that the detachment of smaller droplets requires a higher critical acceleration, as expected. An excellent quantitative match between experiments and simulations is achieved for the silicon surface, and the GDL with 5% and 10% Teflon. However, the predicted result for the GDL with 0% Teflon deviates somewhat from the experiment, especially when large droplets are considered. A possible explanation is that the largest difference between the advancing and receding contact angles (i.e., largest contact angle hysteresis) is measured for the GDL with 0% Teflon. This large contact angle asymmetry causes the droplet to substantially elongate and cover a large test surface, which questions the assumption that the tested material has uniform surface

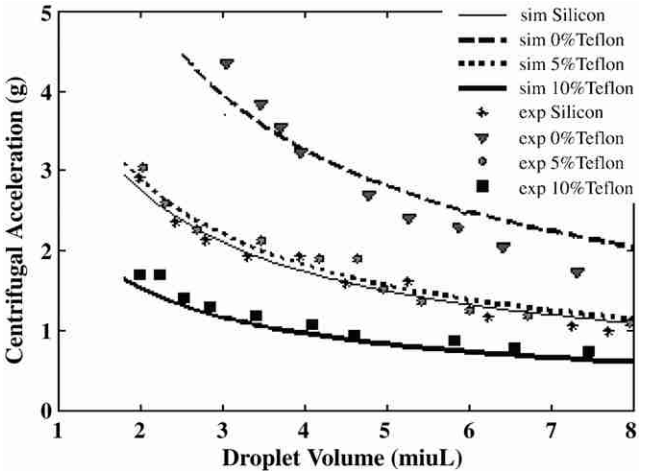

Fig. 12. Critical acceleration as a function of droplet volume for drops on four test materials.

properties. It is also very interesting to note that the centrifugal acceleration-droplet detachment characteristics of the 5% Teflon GDL are very similar to that of the silicon wafer, although the contact angles recorded for both materials are significantly different.

5.2. Liquid slug growth and detachment in a microchannel

The small dimensions and high aspect ratios of the silicon microchannels used here substantially enhance the impact of surface tension and contact angle asymmetry effects, which are favorable for the purposes of model validation. To ensure that the water flow conditions used in our simulation are consistent with those of the experiment, the water injection flow rates are directly extracted from the imaging data by measuring the slug volume change as a function of time, rather than from the reading of the syringe pump. A perfect linear correlation between slug volume and time is found for all cases in our study, which also indicates that slug evaporation is negligible during the growth process due to the small time scale involved, and it is therefore safe to neglect mass diffusion effects in the calculation. In accordance to the wide range of flow conditions tested in the experiment, the current comparison is conducted over nine cases, with the air flow velocities ranging from 13 m/s to 26 m/s. Although the same nominal syringe pump flow rate was used for all the experiments, the effective water injection flow rates measured from the image data differ from case to case, ranging from 0.09 m/s to 0.18 m/s. Hidrovo et al. (2005) shows that under the conditions tested the water injection flow rate influences the slug entrainment frequency but has no significant effects on slug departure size.

As a key feature of our model, the advancing and receding contact angles need to be specified as an input to the simulation. For the microchannel in the experiment, the bottom advancing and receding contact angles are measured from the slug side view to be 105° and 70°, respectively. However, it is difficult to perform the in situ measurement of the contact angles at the side walls since the top view is not available. Furthermore, the manufacturing process can significantly change the surface properties, rendering the ex situ measurements based on the exterior sample surface inapplicable to the interior surface. Therefore, our approach was to run the simulation over a wide range of contact angles values in order to determine which contact angle value yields the most consistent results with the experimental observations. To maximize sensitivity to the side wall contact angle variation, the fitting is conducted for the case with the largest slug detachment length, which corresponds to the flow condition: air: 13.38 m/s, water: 0.11 m/s. In practice, the side wall receding contact angle is first fixed at a reasonable guessed value, say 45°, and various advancing contact angles are tested, which yields a plot indicating the relationship between advancing contact angle values and slug detachment height. Once the advancing contact angle is determined and fixed, a plot of the receding contact angles versus slug detachment length is constructed in the same manner. The fitted values of the side wall advancing and receding contact angles combination are determined by using these plots with the experimentally obtained slug length measurements. Using this fitting method, it is found that the side wall advancing and receding contact angles of 135° and 70°, respectively, generate results that perfectly match the experimental data over the entire the range of flow conditions.

Figs. 13 and 14 show the comparison between experiments and simulations for two flow conditions. In Fig. 13, 15.56 m/s air velocity and 0.09 m/s water velocity are employed, whereas in Fig. 14 the air and water velocities are set to be 17.78 m/s and 0.11 m/s, respectively. The same microchannel is used in both cases, so the same fitted contact angle value is employed in both cases. The first row in each figure corresponds to the non-hysteresis simulation in which the current hysteresis model is not employed and only a single contact angle (105° for Fig. 13 and 90° for Fig. 14) are specified for the entire computational domain. Conversely, the second row depicts the simulation based on the present hysteresis model. The third row shows the experimental results against which our simulations are compared. The white arrow indicates the direction of the airflow, and the bottom water injection slot is located at the lower left corner of each image.

As evidenced in the figures, an excellent quantitative match is achieved between experiment and simulation in the following aspects: (1) the height and length of the liquid slug throughout its growth process and especially at the detachment point, shown in the last image of the 2nd row, turn out to be quite consistent with those in the experiment. The quantitative comparison in terms of this aspect will be conducted over the entire flow conditions in the following discussion. (2) Similar to the experimental observation, the slug growth velocity in the longitudinal direction is much higher than that in the transverse direction, resulting in a elongated shape. (3) The curvature of the

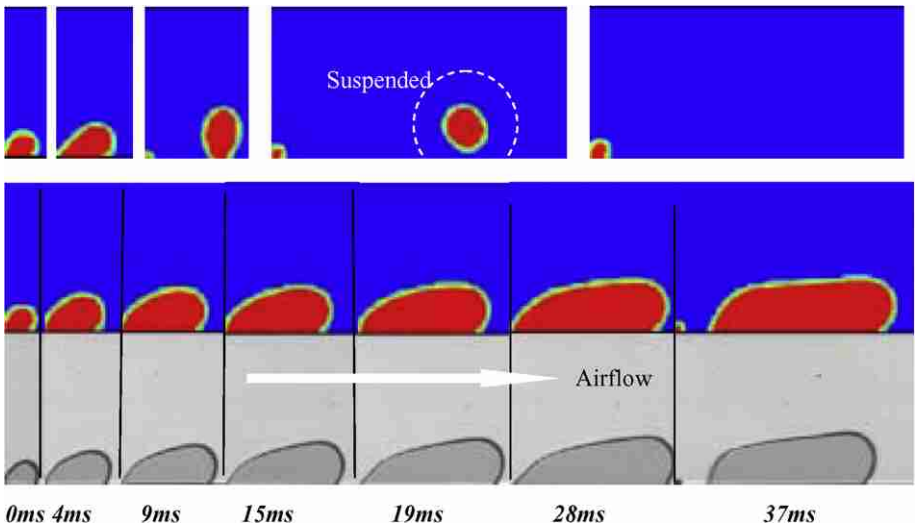

Fig. 13. Comparison for condition A: air: 15.56 m/s, water: 0.09 m/s, side wall 135°/70°, bottom: 105°/70° row 1: simulation without hysteresis, row 2: simulation with hysteresis, row 3: experiment.

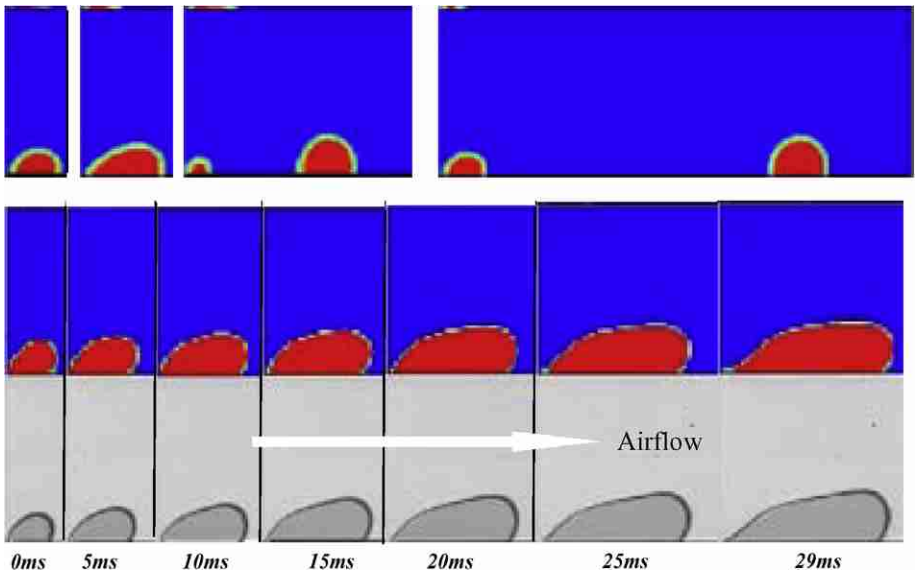

Fig. 14. Comparison of the predicted slug growth process to the experiment for condition B: air: 17.78 m/s, water: 0.11 m/s, side wall 135°/70°, bottom: 105°/70°. Row 1: simulation without hysteresis, row 2: simulation with hysteresis, row 3: experiment.

computed liquid slug profile also varies in a similar pattern as that of the real slug does. Due to the difficulty of experimentally measuring the out of plane curvature, the present comparison is restricted to the liquid slug profile curvature in the plane of the image.

For the non-hysteresis cases shown in Figs. 13 and 14, the liquid slug detachment occurs at 9 ms and 10 ms, respectively, both of which are much earlier than their counterparts in the hysteresis simulation as well as in the experiment. Whenever the hysteresis effect comes into play, the asymmetric distribution of the contact angle along the slug profile gives rises to a net retentive force which resists the slug motion in the streamwise direction, and in turn delays the onset of detachment. Conversely, the absence of the hysteresis precludes the asymmetry of the contact angle distribution and the existence of the retentive force as well, leading to the early detachment. Another characteristic contradiction of the non-hysteresis model with respect to the experiment is that the detached slug without hysteresis tends to contract radially and become circular rather than elongated in the image plane. In reality, such phenomenon typically occurs for droplets in free space, but is not realistic in a confined space due to the impact of the hysteresis effect.

The non-hysteresis simulation in Fig. 13 also shows that the slug eventually detaches from the microchannel bottom and becomes "suspended" (in the plane of the image) in the airflow, which is commonly observed in simulations of

highly hydrophobic microchannels in the absence of hysteresis. As Basu et al. (1997) discussed, a sliding drop detaches when the hydrodynamic lift force exceeds the adhesive forces acting in the normal direction to the microchannel bottom. The lift force originates from the asymmetry of the air flow field over the liquid slug. However, the corresponding adhesive force, which resists the lifting motion of the liquid slug in the microchannel, stems from the interfacial surface tension and is proportional to the sine function of the contact angle, provided the hysteresis effect is neglected. Therefore, since a 90° contact angle yields higher adhesive force than any other contact angle value does, slug lifting never occurs in the non-hysteresis simulation of Fig. 14 with 90° contact angle. It should also be noted that such lifting and suspension never happen when the contact angle hysteresis comes into play. Similar to what occurs in the longitudinal direction, the hysteresis effect also generates a net force in the transverse direction normal to the bottom, which prevents the liquid slug from lifting and becoming suspended.

Fig. 15 shows the comparison between experiment and simulation in terms of the slug critical heights at the detachment point corresponding to various air velocities. Twelve cases were considered over air velocities ranging from 13.38 m/s to 32 m/s and a single combination of bottom/side wall contact angles were used for all the cases. It is shown that the results of the hysteresis model perfectly match the experimental measurements over a wide range of flow conditions, with the maximum relative error less than 10%. It should also be noted that the cases of high air velocity (small detachment height) generally yield larger error than the cases of small air velocity do. The reason is that the slug size at detachment diminishes with air velocity leading to relative larger experimental measurement errors and the need for a finer computational grid to maintain calculation accuracy. Similarly, Fig. 16 shows the comparison in terms of the correlation between slug detachment length and the air velocity. It is evident that the hysteresis model yields much better results (solid line) than the non-hysteresis model does (dashed line).

Due to the high aspect ratio of the channel considered here, the surface adhesion force acting on the side wall dominates the liquid slug detachment and as such the contact angle distribution along the contact line between the slug and side wall plays an important role. Fig. 17 shows the calculated side wall contact angle distribution along the slug profile during slug growth, where the greyness of the line represents the change of angle value from receding angle (135°) to advancing angle (70°). Initially, a uniform distribution of advancing angle exists along the slug profile. With the growth of the liquid slug, the tail of the slug first experiences a decrease in contact angle value. Further slug growth raises the air drag force, causing a gradual propagation of the decrease in contact angle from the tail to the middle part of the liquid slug.

The side wall contact angle distributions at detachment for various flow conditions are shown in Fig. 18. The

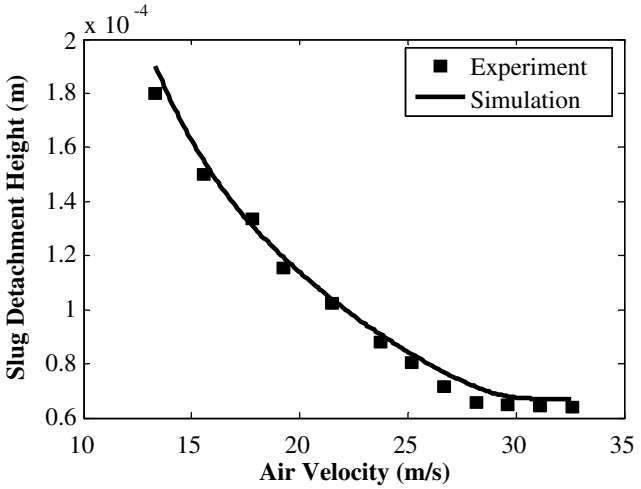

Fig. 15. Comparison of the experimental measurement to the simulation in terms of slug detachment height versus air velocity.

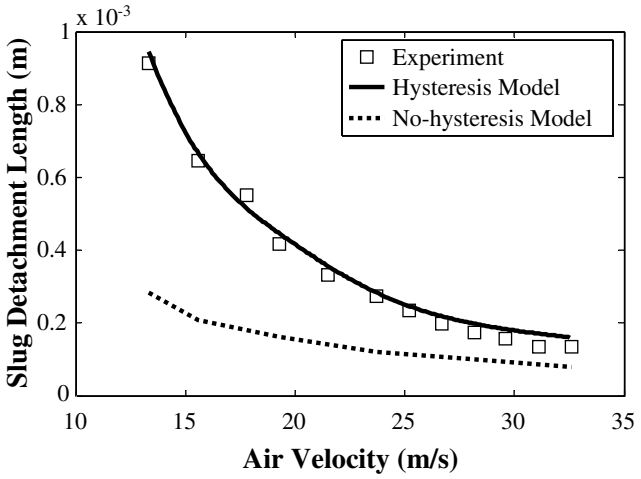

Fig. 16. Slug detachment height versus air velocity. Both hysteresis and non-hysteresis results are presented for the comparison with the experiment.

x-coordinate in the graph represents the curvilinear distance from the point of interest to the liquid slug head, i.e. point F in the legend. The distance has been non-dimensionalized by the entire length of the liquid slug profile from point F to point E. It shows that the angle distributions under various flow conditions share a common combination of characteristic regions, i.e. a uniform advancing angle region, a uniform receding angle region, and a linearly decreasing region in between. If the non-dimensionalized locations of the separation points A and B, which mark the transition from region to region, are compared over cases, some interesting trends arise. Specifically, point B, which marks the transition from a receding contact angle region to a linearly decreasing contact angle region, remains fixed at 0.7 for various air flow rates. Conversely, point A, which marks the transition between the advancing contact angle region and the linearly decreasing contact angle region,

Fig. 17. Predicted side wall contact angle variation during slug growth flow condition: air: 15.56 m/s, water: 0.09 m/s, side wall 135°/70°, bottom: 105°/70°.

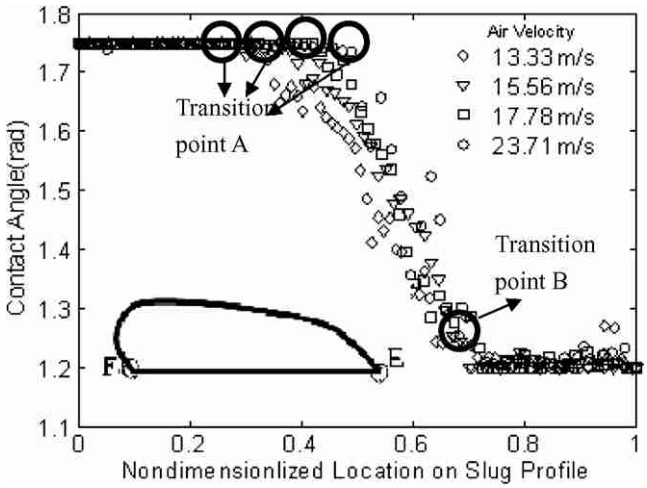

Fig. 18. Predicted side wall contact angle distribution at detachment point for various air velocities and slug detachment lengths.

shifts to the right (aft section of the slug) with increasing air flow rate and consequent decrease in liquid slug detachment size. In other words, the increasing air velocity will narrow the linearly decreasing contact angle region and cause the line AB to become steeper. In their efforts to evaluate the net surface tension acting on the triple line of a bubble or liquid droplet, Blackmore et al. (2001) and Mahe et al. (1988) assumes that the contact angle on the upstream half of the contact line is uniform at the advancing contact angle value and on the downstream half of the contact line is uniform at the receding angle value. Likewise, Brown et al. (1980) and Rotenberg et al. (1984) assumes that the contact angle decrease linearly from the head to the tail, while Basu et al. (1997) assumes that there exists a uniform advancing contact angle region, followed by a linearly decreasing contact angle region that transitions from the advancing contact angle to the receding contact angle. Our simulation results show a distribution pattern different from these works. It should be noted that a portion of the contact line moves prior to detachment. It is discussed previously that the contact angle on a moving contact line can deviate from its equilibrium value θ_A, θ_R in a manner described by Eqs. (3) and (4), i.e., θ can be either higher than θ_A or smaller than θ_R. However, considering that the contact line moves at a very slow velocity before detachment such deviation is not visible in Fig. 18.

An interesting phenomenon observed in both the experiments and simulations is the slug growth and deformation instability after detachment, as illustrated in Fig. 19. Under some flow conditions, a post-detachment slug may experience an abrupt increase in height and decrease in the length such that the liquid slug is squeezed during forward movement. A sudden increase of the slug height causes the air drag force to build up dramatically, resulting in an extremely large acceleration of the slug motion. Such motion pattern is not stable and the liquid slug will eventually break up into small droplets entrained by the air flow. The blurring of the last image in row 1, Fig. 19 is a good illustration of the fairly high velocity of the slug before its break up. In the present simulation, the dynamic contact angle is calculated based on Eqs. (3) and (4). Although a detailed discussion of the mechanism behind the liquid slug instability is beyond the scope of this paper, it is very important to note that the contact angle hysteresis effect is the primary factor that induces the post-detachment slug instability, which never takes place in the absence of the boundary adhesion force caused by the hysteresis effect. Recall that, as was illustrated in Figs. 13 and 14, a non-hysteresis model generally yields a symmetric and round slug shape, which never deforms in an unstable manner.

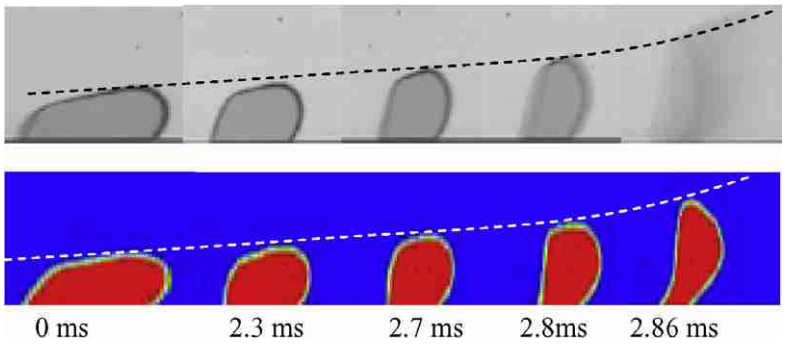

Fig. 19. Slug instability process after detachment for flow condition: air: 17.78 m/s, water: 0.11 m/s, side wall contact angle 135°/70°, bottom contact angle: 105°/70°.

6. Conclusion

Surface tension acting at the triple line is very important in microscale multiphase flows. Specifically, contact angle hysteresis plays a critical role. To account for this factor, the present study focuses on the numerical simulation of liquid–gas microscale multiphase flows using a contact angle hysteresis model based on the VOF model. Solving the non-linear equations accounting for the relationships among volume fraction, interface position, and contact angle, a special model is developed to replicate the hysteresis effect. Moreover, the dynamic contact angle, which is velocity dependent if the contact line is in motion, has been considered by employing an empirical formulation and calculating the displacement of the contact line between consecutive time steps. For validation of the model, two experiments including droplet detachment on a rotating disk and liquid slug flow in a microchannel were conducted, and a systematic comparison between experiments and simulations was performed. In both cases, quantitative matching is achieved for a wide range of flow conditions and the importance of the contact angle hysteresis effect has been clearly illustrated.

Both the simulations and experiments of droplet detachment on a spinning plate reveal that elongation of the contact line generally takes place and the droplet tends to spread on the surface in response to the applied centrifugal acceleration. It is found that the droplet adhesion characteristics of a SAM FTDS coated silicon surface resemble that of a GDL with 5% Teflon. This implies that materials with different surface properties can yield quite similar adhesive or retentive interactions with liquids such as water provided the combinations of advancing and receding contact angles are alike.

The simulation of the slug flow in a microchannel shows the contact angle hysteresis is responsible for the slug elongation and the post-detachment instability. In addition, the simulation result implies that contact angle distribution along the slug profile can be approximated using piecewise linear functions. Moreover, considering that the multiphase flow patterns arising in a confined space at the microscale are extremely sensitive to surface properties, the present contact angle hysteresis model can be used to estimate the surface properties for which an in situ measurement is difficult to conduct. For example, the advancing and receding contact angles of a microchannel can be estimated by identifying the optimal contact angle values that provide the best match between the computed flow pattern and the experimental observations. A similar approach has been used by Wang et al. (2006) for the prediction of bubble geometry.

Finally, excellent agreement of the calculated liquid slug dimensions at detachment with those measured in the experiment shows the potential of the current model to predict slug growth and detachment behavior in microchannels, a problem of great importance in a wide range of engineering applications such as fuel cell water management and microfluidic devices.

Acknowledgements

The authors are grateful for the support of this work by Stanford Graduate Fellowship and Honda R&D Co. Ltd. Silicon microchannels used in the present study were fabricated at the Stanford Nanofabrication Facility (a member of the National Nanofabrication Users' Network) which is supported by the National Science Foundation under Grant ECS-9731293. The authors also would like to thank Applied Microstructures Inc. for their chip coating services.

References

Barajas, A.M., Panton, R.L., 1992. The effect of contact angle on two-phase flow in capillary tubes. Int. J. Multiphase Flow 19, 337.

Basu, S., Nandakumar, K., Masliyah, J., 1997. A model for detachment of a partially wetting drop from a solid surface by shear flow. J.Colloid Interface Sci. 190, 253.

Bikerman, J.J., 1965. Journal of Colloid Science. Academic Press, p. 349.

Blackmore, B., Li, D., Gao, J., 2001. Detachment of bubbles in slit microchannels by shearing flow. J. Colloid Interface Sci. 241, 514–520.

Brackbill, J.U., Kothe, D.B., Zemach, C., 1992. A continuum method for modeling surface tension. J. Comput. Phys. 100, 335–354.

Brown, R.A., Orr, F.M., Scriven, L.E., 1980. Static drop on an inclined plate: analysis by the finite element method. J. Colloid Interface Sci. 73, 76–87.

Cha, S.W., Lee, S.J., Park, Y.I., and Prinz, F.B., 2003. Investigation of transport phenomena in micro flow channels for miniature fuel cells. In: Proceedings of the First International Conferences on Fuel Cell Science, Engineering and Technology, April 21–23, New York, pp.143–148.

Chen, Y., Kulenovic, R., Mertz, R., 2008. Numerical study on the formation of Taylor bubbles in capillary tubes. Int. J. Thermal Sciences, in press.

Concus, P., Finn, R., 1974. On capillary free surfaces in the absence of gravity. Acta Math. 132, 177–198.

Crynes, L., Cerro, R.L., Abraham, M.A., 1996. The monolith froth reactor: development of a novel three-phase reactor. A.I.Ch.E., J. 41, 337–345.

Dussan, E.B., 1979. On the spreading of liquids on solid surfaces: static and dynamic contact angles. Ann. Rev. Fluid Mech. 11, 371–400.

Feng, Z., Serizawa, A., 2000. Two-phase flow patterns in ultra-small channels. In: Second Japanese–European Two-phase Flow Group Meeting, Tsukuba, Japan.

Francois, M., Shyy, W., 2003. Computations of drop dynamics with the immersed boundary method, Part 2: drop impact and heat transfer. Numer. Heat Transfer Part B 44, 119–143.

Gregor, C., Stojan, P., Lztok, T., 2001. Coupling of the interface tracking and the two-fluid models for the simulations of incompressible two phase-flow. J. Comput. Phys. 171, 776–804.

Hidrovo, C., Wang, F., Steinbrenner, J., Lee, E., Vigneron, S., Cheng, C., Eaton, J., Goodson, K., Experimental investigation and visualization of two-phase flow and water transport in microchannels, 2004. In: Proceedings of IMECE 2004: 2004 ASME International Mechanical Engineering Congress and RD&D Expo, Anaheim, California, USA.

Hidrovo, C., Wang, F., Steinbrenner, J., Lee, E., Vigneron, S., Cheng, C., Eaton, J., Goodson, K., 2005. Water slug detachment in two-phase hydrophobic microchannel flows. In: Proceedings of ICMM 2005: Third International Conference on Microchannels and Minichannels, Toronto, Ontario, Canada.

Issa, R.I., Gosman, A.D., Watkins, A.P., 1991. The computation of compressible and incompressible recirculating flows by a non-iterative implicit scheme. J. Comput. Phys. 93, 388–410.

Jiang, T.-S., Oh, S.-G., Slattery, J.C., 1979. Correlation for dynamic contact angle. J. Colloid Interface Sci. 69, 74.

Mahe, M., Vignes-Adler, M., Rousseau, C., Jacquin, C.G., Adler, P.M., 1988. Adhesion of droplets on a solid wall and detachment by a shear flow. J. Colloid Interface Sci. 126 (1), 314–328.

Peng, X.F., Wang, B.X., 1993. Forced-convection and flow boiling heat transfer for liquid flow through micro-channels. Int. J. Heat Mass Transfer 36, 3421–3427.

Renardy, M., Renardy, Y., Li, J., 2001. Numerical simulation of moving contact line problems using a volume-of-fluid method. J. Comput. Phys. 171, 243–263.

Rotenberg, Y., Boruvka, L., Neumann, 1984. The shape of nonaxisymmetric drops on inclined planar surfaces. J. Colloid Interface Sci. 102, 424–434.

Scardovelli, R., Zaleskiy, S., 2000. Analytical relations connecting linear interfaces and volume fractions in rectangular grids. J. Comput. Phys. 164, 228–237.

Taha, T., Cui, Z.F., 2004. Hydrodynamics of slug flow inside capillaries. Chem. Eng. Sci. 59, 1181–1190.

Tanner, L.H., 1979. The spreading of silicone oil drop on horizontal surfaces. J. Phys. D: Appl. Phys. 12, 1473–1484.

Theodorakakos, A., Ous, T., Gavaises, M., Nouri, J.M., Nikolopoulos, N., Yanagihara, H., 2006. Dynamics of water droplets detached from porous surfaces of relevance to PEM fuel cells. J. Colloid Interface Sci. 300, 673–687.

Tseng, F.G., Yang, I.D., Lin, K.H., Ma, K.T., Lu, M.C., Tseng, Y.T., Chieng, C.C., 2002. Fluid filling into micro-fabricated reservoirs. Sensors Actuators A 97–98, 131–138.

Wang, E., Devasenathipathy, S., Lin, H., Hidrovo, C., Santiago, J., Goodson, K., Kenney, T., 2006. A hybrid method for bubble geometry reconstruction in two-phase microchannels. Exp. Fluids 40, 847–858.

Youngs, D.L., 1982. Time-dependent multi-material flow with large fluid distortion. In: Morton, W., Baines, M.J. (Eds.), Numerical Methods for Fluid Dynamics. New York Academic Press, pp. 273–285.

Zhang, L., 2000. Measurements and modeling of two-phase flow in microchannels with nearly-constant heat flux boundary conditions. In: Proceeding of Micro-Electro-Mechanical Systems (MEMS)-2000, pp. 129–135.